Near surface properties derived from Phobos transits with HP RAD³ on InSight, Mars

Nils T Mueller[1], Sylvain Piqueux[2], Mark T Lemmon[3], Justin N. Maki[4], Ralph D. Lorenz[5], Matthias Grott[6], Tilman Spohn[7], Suzanne E. Smrekar[2], Joerg Knollenberg[6], Troy L. Hudson[2], Christian Krause[8], Ehouarn Millour[9], Forget Francois[10], Matthew P. Golombek[11], Axel Hagermann[12], Nicholas Attree[13], Matthew Adam Siegler[14], and William Bruce Banerdt[2]

[1]German Aerospace Center (DLR), Institute of Planetary Research
[2]Jet Propulsion Laboratory
[3]Space Science Institute
[4]Jet Propulsion Laboratory, California Institute of Technology
[5]Johns Hopkins University Applied Physics Lab
[6]DLR Institute for Planetary Research
[7]Institute of Planetary Research
[8]DLR Institute of Space Systems
[9]Laboratoire de Meteorologie Dynamique
[10]LMD
[11]California Institute of Technology/JPL
[12]Lulea University of Technology
[13]University of Stirling
[14]Planetary Sciences Institute

November 22, 2022

Abstract

We use the surface temperature response to Phobos transits as observed by a radiometer on board of the InSight lander to constrain the thermal properties of the uppermost layer of regolith. Modeled transit lightcurves validated by solar panel current measurements are used to modify the boundary conditions of a 1D heat conduction model. We test several model parameter sets, varying the thickness and thermal conductivity of the top layer to explore the range of parameters that match the observed temperature response within its uncertainty both during the eclipse as well as the full diurnal cycle. The measurements indicate a thermal inertia of 103^{+48}_{-24} $Jm^{-2}K^{-1}s^{-1/2}$ in the uppermost layer of 0.2 to 4 mm, significantly smaller than the thermal inertia of 200 $Jm^{-2}K^{-1}s^{-1/2}$ derived from the diurnal temperature curve. This could be explained by larger particles, higher density, or a very small amount of cementation in the lower layers.

Near surface properties derived from Phobos transits with HP^3 RAD on InSight, Mars

N. Mueller[1], S. Piqueux[2], M. Lemmon[3], J. Maki[2], R. D. Lorenz[4], M. Grott[1], T. Spohn[1,5], S.E. Smrekar[2], J. Knollenberg[1], T.L. Hudson[2], C. Krause[6], E. Millour[7], F. Forget[7], M. Golombek[2], A. Hagermann[8], N. Attree[9], M. Siegler[10], and W.B. Banerdt[2]

[1]Institute of Planetary Research, German Aerospace Center (DLR), Berlin, Germany
[2]Jet Propulsion Laboratory, California Institute of Technology, Pasadena, CA, USA
[3]Space Science Institute, College Station, TX, USA
[4]Johns Hopkins Applied Physics Laboratory, Laurel, MD, USA
[5]International Space Science Institute (ISSI), Bern, Switzerland
[6]Microgravity User Support Center, German Aerospace Center (DLR), Cologne, Germany
[7]Laboratoire de Météorologie Dynamique (LMD/IPSL), Sorbonne Université, Centre National de la Recherche Scientifique, École Polytechnique, École Normale Supérieure, Paris, France
[8]Luleå University of Technology, Space campus, Kiruna, Sweden
[9]Faculty of Natural Sciences, University of Stirling, Stirling, UK
[10]PSI, SMU Earth Science, Dallas, TX, USA.

Key Points:

- The surface temperature response to Phobos transits was observed and interpreted
- The thermal inertia of the uppermost layer of soil is $103^{+48}_{-24}\,\mathrm{J\,m^{-2}\,K^{-1}\,s^{-1/2}}$
- The thermal conductivity or density of the top 0.2 to 4 mm is significantly less than that of the top 4 cm

Corresponding author: N. Mueller, nils.mueller@dlr.de

Abstract

We use the surface temperature response to Phobos transits as observed by a radiometer on board of the InSight lander to constrain the thermal properties of the uppermost layer of regolith. Modeled transit lightcurves validated by solar panel current measurements are used to modify the boundary conditions of a 1D heat conduction model. We test several model parameter sets, varying the thickness and thermal conductivity of the top layer to explore the range of parameters that match the observed temperature response within its uncertainty both during the eclipse as well as the full diurnal cycle. The measurements indicate a thermal inertia of $103\,^{+48}_{-24}\,\mathrm{J\,m^{-2}\,K^{-1}\,s^{-1/2}}$in the uppermost layer of 0.2 to 4 mm, significantly smaller than the thermal inertia of $200\,\mathrm{J\,m^{-2}\,K^{-1}\,s^{-1/2}}$ derived from the diurnal temperature curve. This could be explained by larger particles, higher density, or a very small amount of cementation in the lower layers.

1 Introduction

Observations of the brightness temperature in response to changes in insolation constrain the thermophysical properties of the upper layer of planetary surfaces, most frequently reported as thermal inertia (TI) defined as the root of the product of volumetric heat capacity ρc and thermal conductivity k. The thermal conductivity constrains the particle size of regolith (Presley & Christensen, 1997a, 1997b, 1997c; Piqueux & Christensen, 2009a) but is also highly sensitivity to cementation (Piqueux & Christensen, 2009b). The depth of regolith that can be probed is approximately the diurnal skin depth $d = \sqrt{k\,D/(\pi\rho c)}$, which is approximately 4 cm for the InSight landing site when adopting the volumetric heat capacity $\rho c = 8.2 \cdot 10^5 \mathrm{JK^{-1}m^{-3}}$ from Morgan et al. (2018) and thermal conductivity k according to the orbiter derived TI of the InSight landing site of 200 $\mathrm{J\,m^{-1}\,K^{-1}\,s^{-1/2}}$ (Golombek, Warner, et al., 2020). If the diurnal temperature curve of the same location is sampled at sufficiently separate local times, typically using in-situ observations (Fergason et al., 2006; Hamilton et al., 2014) instead of sun-synchronous orbiters, it is also possibly to infer layering within the diurnal skin depth (Vasavada et al., 2017; Edwards et al., 2018; Piqueux et al., 2021).

Based on orbiter observations, Golombek et al. (2017) state that the TI of the InSight landing ellipse derived from orbit (200 $\mathrm{J\,m^{-1}\,K^{-1}\,s^{-1/2}}$) is "consistent with a surface composed of cohesionless sand size particles or a mixture of slightly cohesive soils (cohesions of less than a few kPa)" covered by a coating of surface dust responsible for the high albedo of 0.24, which is too thin to affect the diurnal curve. The landing site features TI in the lower range of the landing ellipse (Golombek, Warner, et al., 2020; Golombek, Kass, et al., 2020; Piqueux et al., 2021), however the Heatflow and Physical Properties Package (HP^3) mole (Spohn et al., 2018), although designed and tested for such material, failed to deploy its instrumented tether to the subsurface (Fig. 1). The mole is designed to measure thermal conductivity and the results at its current position in the top 40 cm of regolith are consistent with the observed TI (Grott et al., 2021; Piqueux et al., 2021). The steep wall of the pit created by the penetration attempt, and clasts embedded therein, have been interpreted as evidence for a duricrust (Golombek, Warner, et al., 2020), i.e. that the bonds between grains are strengthened by a cementing material. This raises the question whether the particles are smaller than thought, since such cementation has the potential to strongly increase the thermal conductivity (Piqueux & Christensen, 2009b).

In addition to the derivation of thermophysical properties from the diurnal response, it is also possible to use insolation changes with shorter timescales to probe shallower depths of the material. Transits of the Martian moons, which eclipse a significant fraction of the Sun's disc, provide a shorter stimulus. Phobos transits, with a typical duration of 20 to 30 s, have a skin depth d of 0.3 to 0.8 mm, assuming a thermal conductivity of 0.01 to 0.05 $Wm^{-1}K^{-1}$ corresponding to dust and fine sands, respectively (Presley & Christensen, 1997b). This change in temperature in response to a Phobos transit has been observed by the Thermoskan instrument on the 1989 Phobos mission (Betts et al., 1995). The THEMIS instrument on the Mars Odyssey orbiter observed the Phobos shadow but could not resolve the temperature response (Piqueux & Christensen, 2012). At the InSight landing site the effect of several Phobos transits were observed with different geophysical instruments(Stähler et al., 2020) including the SEIS Very Broad Band seismometer and the infrared radiometer (RAD) of the HP^3 instrument (Spohn et al., 2018; Mueller et al., 2020).

InSight's rocket assisted landing has reduced the albedo locally by removal of the surficial dust layer (Golombek, Warner, et al., 2020). Though some dust might have been shielded behind topographic highs (see Fig.19 in Golombek, Kass, et al., 2020), the reduction in albedo indicates that the remaining top material particles are coarser than that of the aeolian dust. Based on the footprints of the HP^3 support structure and interactions with the robotic arm scoop it is also interpreted as unconsolidated, uncemented

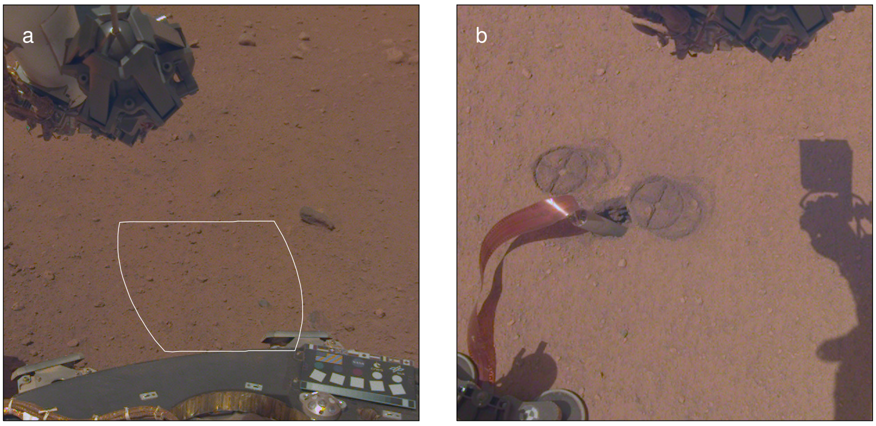

Figure 1. Panel a) outlines the area observed by the radiometer used in this study in a portion of image D001L0010_597418893CPG_F0004C0010M2. Panel b) shows the situation of the HP^3 mole on sol 230 (D006L0230_616943645CPG_F0505_0080M8), after the support structure initially holding the mole has been removed. The hole created by the penetration attempts indicates that the regolith has sufficient strength to support vertical or even overhanging walls, possibly with clasts embedded.

material (Golombek, Warner, et al., 2020). Observing the temperature response to the transit therefore has the potential to characterize material that is similar to the particle size of bulk regolith, but is known to not be cemented.

2 Phobos transits

HP^3-RAD acquired data at the maximum sampling rate of $\approx$0.5 Hz during six transits of the Mars moon Phobos. These transits occurred on sols 96, 97, 99, 498, 499 and 501. To interpret the temperature response it is necessary to quantify the change in insolation during these transits. The most direct measurement of insolation variation can be obtained from recordings of the solar panel currents (Lorenz et al., 2020). During the first three transits the solar panels acquired data only once per 30 s, while later the sampling rate was increased to 0.25 Hz.

To provide lightcurves at sufficient time resolution to model the temperature response, we use the limb finding routine of the SPICE toolkit (Acton, 1996; Acton et al., 2018) to generate series of simulated images of the transits. The shape model of Phobos used in this step was created by Willner et al. (2014). The Phobos position is cal-

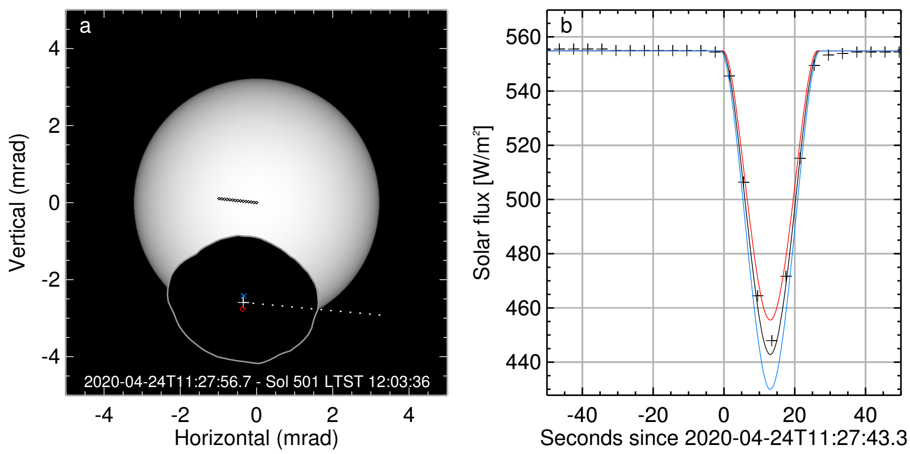

Figure 2. Panel a) shows a simulated image of the outline of Phobos obscuring the disc of the sun at the moment of closest approach. The relative brightness is shown as greyscale. Shown as blue cross and red diamond here are offsets of 1 km along Phobos' rotation axis towards N and S, respectively. Panel b) shows a model of the downwelling visible solar flux in comparison to scaled solar panel currents (+ symbols). The blue and red lightcurves correspond to the offset in Phobos position outlined in panel a) in the same colors.

culated using the ephemerides SPICE kernels 'mar97s.bsp' together other kernels from the InSight collection. The solar limb darkening function is taken from Neckel and Labs (1994) for the solar spectrum maximum at 550 nm. The variation of limb darkening in the visible band from 440 to 880 nm does not significantly change the results. A frame at the closest angular separation for sol 501 is shown in Fig. 2 a.

The aggregate brightness of all pixels of each frame is divided by the aggregate brightness of a frame where Phobos does not obscure any part of the solar disk to generate the curve of relative insolation. This is multiplied with the downwelling visible flux generated by the KRC model (Kieffer, 2013) for the appropriate season and local time, as well as the dust opacity as derived from camera observations (Banfield et al., 2020, e.g.), more details about the model input parameters are in section 3.

The position uncertainty of Phobos results in an uncertainty of the lightcurves. The error of closest angular separation of Sun and Phobos (and thus the amplitude of the insolation loss) is mostly determined by the position error along the normal of Phobos' orbital plane, closely aligned with its rotation axis. Recent work by Lainey et al. (2020) shows out of plane position differences to the mar97 ephemerides on the order of 1 km and we adopt this value as out-of-plane error as a worst case assumption. The change in apparent Phobos position at closest separation to the sun and the corresponding variation in the lightcurve is presented in Fig. 2.

The solar array current is scaled with a conversion factor specific to each transit so that the scaled flux matches the modeled visible flux directly before the transit. The modeled lightcurves and solar panel data are shown for sol 501 in Fig. 2 b. The equivalent plots for all transits are shown in the supplement. Solar array data and modeled lightcurves fit well within the adopted uncertainty, with exception of sols 99 and 498. The bad fit of these transits occurring late in the afternoon is likely a result of scattering and refraction in the atmosphere, as discussed in Stähler et al. (2020). This appears to reduce the effect of the eclipses although at solar elevations greater or equal to that of sol 499 (34°) the deviation is within the uncertainty from the position of Phobos. Table 1 provides the solar elevation angle for the different transits.

3 Transit temperature response

The temperatures observed by the HP^3 radiometer during the transit and the diurnal temperature curves of sol 501 are shown in Fig. 3, with the corresponding plots of all transits shown in the supplement. The total uncertainty of the RAD measurements is dominated by potential calibration errors (Mueller et al., 2020), which do not change significantly over the period of the eclipse. The observation of the amplitude of the transit response is therefore better characterized by the quasi-random variability that we attribute to variable winds disturbing the instrument. To quantify this error we search the 10 minutes of 0.5 Hz data prior to the transit for the largest temperature difference within a running window equal to the duration of the transit. The diurnal trend is removed by subtracting a linear fit to the whole 10 minutes. This maximum temperature difference over the duration equivalent to that of the transit σT_{obs} is adopted as error estimate relevant to the transit response amplitude and plotted as error bars in Fig. 3 a. This error is different for each event, likely due to different wind conditions.

To interpret the measurements we model surface temperatures based on the external boundary conditions, i.e. incident visible and infrared fluxes, calculated with the KRC model (Kieffer, 2013) using the regional average albedo of 0.25 and TI of $200\,\mathrm{J\,m^{-2}\,K^{-1}\,s^{-1/2}}$ (Golombek et al., 2017) as well as the visible wavelength atmospheric dust opacity τ derived from sky imaging (Banfield et al., 2020) as input parameters (Table 1). The dust optical properties are the same as in the work of Piqueux et al. (2021) based on the work of Vasavada et al. (2017). The visible flux is modified with the relative transit lightcurves, as shown in Fig. 2. The diurnal temperature curves of the same subsurface model show differences to the observed temperatures that appear to be a function of season, resulting in an apparent variation of the best fitting bulk TI. We address this by adding 9 W to the IR fluxes of the second set of transits. This value is similar to the maximum amplitude of additional IR flux that Vasavada et al. (2017) add as a function of season to their model fitting ground temperatures observed by the radiometer on the Curiosity rover (Gómez-Elvira et al., 2012). Vasavada et al. (2017) interpret this missing flux as an effect of seasonal clouds that were not included in the model.

We solve the heat conduction equation using the implicit Euler method, which allows us to more freely vary the time and depth steps since this method is numerically unconditionally stable. The discretization scheme is based on the scheme described in the work of Kieffer (2013) and our modified equations are provided in the supplementary material. The numerical layer thicknesses are 0.1 mm in the upper mm and double in thickness at each layer below that. Time steps are 1000 s except for the period around the eclipses, when time steps are reduced to 0.5 s. The modeled temperature response to the transit shows little sensitivity to time and depth step size as long as they are smaller than 0.5 s and 0.2 mm, respectively.

The models shown in Fig. 3 differ mostly only in the thermal conductivity k_1 of the upper layer of the regolith, as well as the thickness layer z_1. All models use a density $\rho = 1300\text{kg/m}^3$ and a specific heat capacity $c_p = 630\text{J/kg}$ as recommended by Morgan et al. (2018). The values of thermal conductivity and heat capacity are provided for the reference temperature of 220 K and their temperature dependence in the model follows the approximations recommended by Morgan et al. (2018). The albedo is assumed to be $a = 0.16$, which both matches the estimate of a 35% darker lander blast zone than the regional average ($a = 0.25$) as well as the observed surface temperatures (Golombek, Warner, et al., 2020; Piqueux et al., 2021).

The models were adjusted by visually matching the resulting temperatures to the observations during the eclipse and over the sol of the eclipse. The aim of this manual fitting was first to generate model curves that match the amplitudes of the eclipse and

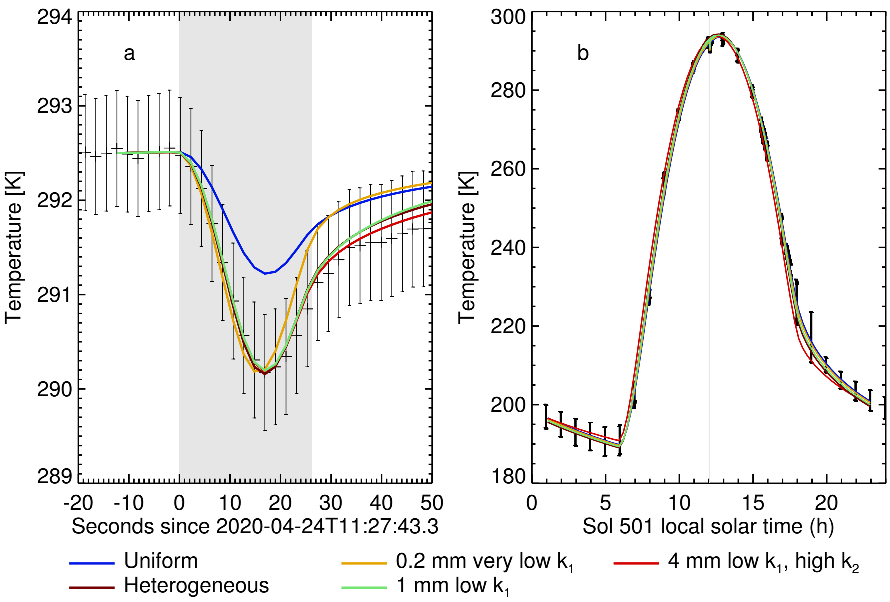

Figure 3. Measured and modeled surface temperatures near the transit on sol 501. a) the temperature response to the transit in detail with error bars derived from the data directly before the transit as described in the text. An offset is subtracted from each model to match the data in the 20 s before the transit. b) shows the diurnal temperature curve with error bars corresponding to the total measurement uncertainty.

diurnal response, and second to remain within the interval of uncertainty at all times. Finding an optimal fit with the least squares method as done by (Piqueux et al., 2021) would require a trade-off in weight of the two data selections, since comparatively few data points contain information about the eclipse response. We found that the outcome of this fit varied strongly depending on the choice of the weight. Thus we considered it more instructive to directly compare several models that bracket the parameter space that can fit the data reasonably well.

Uniform: The subsurface is a homogeneous half space with a thermal conductivity of 50 $\mathrm{mW\,m^{-1}\,K^{-1}}$, corresponding approximately to the bulk TI of 200 $\mathrm{J\,m^{-2}\,K^{-1}\,s^{-1/2}}$ derived from the diurnal curves by Golombek, Warner, et al. (2020). This model results in a transit response too small for those sols where the insolation dip is well understood (sol 96, 97, 499, 501). In case of the sol 501 transit, shown in Fig. 3, the model curve falls outside of the observation error bar. The model matches the diurnal temperature measurements very well (Fig. 3 b), indicating that the top layer causing the deeper transit response is thin compared top the diurnal skin depth of 4 cm, as discussed more detail by Piqueux et al. (2021).

0.2 mm very low $\mathbf{k}_1$. This model intends to represent a very thin layer of fine aeolian dust with an effective thermal conductivity of only k_1=8 $\mathrm{mW\,m^{-1}\,K^{-1}}$ (TI 81 $\mathrm{J\,m^{-2}\,K^{-1}\,s^{-1/2}}$). The half space below has a thermal conductivity of 50 $\mathrm{mW\,m^{-1}\,K^{-1}}$, matching the diurnal TI. This model fits the diurnal curve similarly well as the homogeneous model, and matches the amplitude of the observed temperature drop during the transit on sol 501. The shape of the transit response overall is however not a good match, the minimum occurs too early and the return to pre-transit temperatures is too fast.

4 mm low $\mathbf{k}_1$. This model aims to represent geologic interpretations where a layer of unconsolidated regolith several mm thick (Fig. 1) overlies some consolidated material with sufficient strength to support a near vertical wall with embedded clasts (Fig. 1 b). The depth of the hardware footprints is at least several mm so that a thickness of 4 mm is adopted. The temperature drop of the transit on sol 501 is fitted by choosing a thermal conductivity of k_1=13 $\mathrm{mW\,m^{-1}\,K^{-1}}$ (TI 103 $\mathrm{J\,m^{-2}\,K^{-1}\,s^{-1/2}}$). This top layer is sufficiently thick to significantly affect the diurnal temperature curve and the lower half space thermal conductivity is increased to 80 $\mathrm{mW\,m^{-1}\,K^{-1}}$ (TI 255 $\mathrm{J\,m^{-2}\,K^{-1}\,s^{-1/2}}$) to approximately match the observed diurnal amplitude. Increasing the top layer thickness further, or decreasing the lower half space thermal conductivity, does not significantly affect the transit temperature minimum, and only slightly reduces the post-transit temperatures. The temperatures recorded after the transit on sol 501 (Fig. 3 a) seem to indicate a top layer thicker than 4 mm, but this can be ruled out by comparison to the diurnal data (see also Piqueux et al., 2021). The 4 mm top layer already cools too fast in the afternoon and evening just so that model temperatures fall outside of the total measurement error bar around 19 h local true solar time (LTST) (Fig. 3 b).

1 mm low $\mathbf{k}_1$. The top layer thickness can be bounded to 0.2 mm $< z_1 <$ 4 mm by requiring the model to match the observed transit response and the diurnal curve within their respective error estimates. The best constraint is provided by the transit on sol 501 (Fig. 3). For comparison of the different transits we adopt a top layer thickness of 1 mm, which matches measurements on sol 501 well and derive the layer's thermal conductivity by matching this model to each observation. The best constraint is provided by the

Sol	LTST	$e_{\text{sol}}[°]$	t_{ecl} [s]	τ	ΔT_{min}[K]	σT_{obs}[K]	σT_{pos}[K]	$k_1[\frac{\text{mW}}{\text{m}\cdot\text{K}}]$	ΔT_{mod}[K]
96	13:06	71	24.3	1.05	1.22	0.95	0.22	19^{+52}_{-15}	-1.37
97	11:15	76	26.7	1.04	1.82	1.19	0.26	25^{+38}_{-17}	-2.22
99	15:53	31	20.1	0.94	0.41	0.28	0.08	7^{+69}_{-3}	-0.74
498	17:24	8.6	34.8	0.69	0.40	0.17	0.005	26^{+50}_{-19}	2.50
499	15:41	34	25.4	0.73	0.78	0.32	0.11	12^{+43}_{-8}	-0.54
501	12:03	82	26.3	0.70	2.33	0.61	0.29	13^{+15}_{-6}	-0.39

Table 1. Eclipse parameters and derived thermal conductivity assuming a 1 mm top layer. The observed transits differ in solar elevation e_{sol}, duration t_{ecl}, visible wavelength dust opacity τ, observed temperature difference between start and minimum during the transit ΔT_{min}, assumed error of temperature observation σT_{obs}, temperature equivalent of the assumed error in flux variation due to Phobos position uncertainty σT_{pos}, which results in variations of the fitted thermal conductivity of the top layer k_1 and its uncertainty. The difference of the fitted diurnal curve to the measurements at start of the transit are provided under ΔT_{mod}.

maximum temperature drop over the transit ΔT_{min}, which is relatively unaffected by top layer thickness or lower half space parameters.

We assume that this value can be affected by measurement errors (σT_{obs}). The models on the other hand are affected by the uncertainty in the position of Phobos, as outlined in the plot of lightcurves (Fig. 2). For easier comparison we express this as temperature difference of the transit temperature minimum (σT_{pos}) calculated with the nominal model parameters and the different lightcurves. The impact of the Phobos position error is generally smaller than that of the measurement. We add these error contributions quadratically and derive the thermal conductivities that result in the temperature drop ΔT_{min} modified by these errors in order to estimate the uncertainty.

The thermal conductivities derived from the different transits are consistent with the best constraint from sol 501. The best fitting value is the same as when assuming a 4 mm layer, k_1=13 mW m^{-1} K^{-1} (TI 103 J m^{-2} K^{-1} s$^{-1/2}$). There could be a trend of decreasing thermal conductivity over time but the uncertainties are too large, especially considering that the Phobos position error is likely a function of time and similar for the pairs of transits of sol 96/97 and sol 499/501.

Heterogeneous. We explore the possibility that pockets of low thermal conductivity material (i.e. aeolian dust) survived the landing rocket blast in topographic lows or the lee of clasts. To this end we assumed that half of the observed surface area responds like the uniform model, and that the other half has a 1 mm thick top layer with a thermal conductivity of k_1=6 $\mathrm{mW\,m^{-1}\,K^{-1}}$ (TI 70 $\mathrm{J\,m^{-2}\,K^{-1}\,s^{-1/2}}$), again chosen to match the temperature minimum of the transit. This model fits both the transit and diurnal curve well in all transits with high solar elevation. Clasts with diameters >20 mm cover a cumulative fractional area of of 2.5 % (Golombek, Warner, et al., 2020) so that it is unlikely that the clasts themselves significantly affect the average response of the observed area.

4 Discussion and conclusions

The transit response indicates that the thermal properties of the topmost millimeter of regolith are different from those of the underlying material within the diurnal skin depth of 4 cm. The thickness of this top layer is between 0.2 and 4 mm, bounded by the shape of the transit response and the diurnal curve, respectively. A thickness of 1 mm fits both the transit and the diurnal response well. Assuming a topmost layer thickness of 1 mm and uniform layer properties, the best constraint on top layer thermal conductivity is 13^{+15}_{-6} $\mathrm{mW\,m^{-1}K^{-1}}$, which corresponds to a TI of 103^{+48}_{-24} $\mathrm{J\,m^{-2}\,K^{-1}\,s^{-1/2}}$. At this thickness, the thermal conductivity of the lower half space does not significantly affect the transit response.

The diurnal curves studied here are consistent with the underlying half space thermal conductivity of 50 $\mathrm{mW\,m^{-1}K^{-1}}$, consistent with the TI of 200 ±30 $\mathrm{J\,m^{-2}\,K^{-1}\,s^{-1/2}}$ from the work of Golombek, Warner, et al. (2020) and the more detailed study of the data up to sol 50 by Piqueux et al. (2021) which arrives at 183 ± 25 $\mathrm{J\,m^{-2}\,K^{-1}\,s^{-1/2}}$. The $\mathrm{HP^3}$ mole, embedded in the top 37 cm of soil of a location within 6 m distance, measures a thermal conductivtiy of $39 \pm 2\,\mathrm{mW\,m^{-1}\,K^{-1}}$, corresponding to a TI of $178 \pm 4\,\mathrm{J\,m^{-2}\,K^{-1}\,s^{-1/2}}$ (Grott et al., 2021). The cause of the discrepancy between the lower layer TI of 200 $\mathrm{J\,m^{-2}\,K^{-1}\,s^{-1/2}}$ in this work, fitted to the diurnal data close to sol 100, to the TI of 183 $\mathrm{J\,m^{-2}\,K^{-1}\,s^{-1/2}}$ fitted to diurnal data before sol 50, is not clear yet. Both estimates use the same model for incident visible and infrared fluxes (Kieffer, 2013). One possibility might be that the dust storm arriving after sol 50 (Viúdez-Moreiras et al., 2020) has changed the optical properties of the dust aerosols (Lemmon et al., 2019), which were kept constant in our modeling. The discrepancy necessitating the offset of 9 W in the energy budget between sol 100 and 500, equivalent to a further increase in apparent TI, could be caused by seasonally occurring clouds (Vasavada et al., 2017). We anticipate that the long term observation of an unchanged surface location in combination with the meteorological sensors of InSight will improve our understanding of the seasonal variation of the surface energy budget, including smaller terms such as the sensible heat flux (Spiga et al., 2021). A further study of this is however beyond the scope of this paper as the main conclusion of a low thermal inertia at the surface layer is not affected by this uncertainty.

The thermal conductivity we derive for the top layer is approximately 2 to 4 times lower than that of the underlying material, i.e. a TI contrast of approximately 1.4 to 2. This is similar to the results of Betts et al. (1995) who derive a TI from the Phobos transit observation that is up to two times smaller than the diurnal TI. This contrast is consistent with smaller grain size or less cementation in the top layer (Presley & Christensen, 1997c; Piqueux & Christensen, 2009b), although this is not a necessary conclusion from our observations. The most likely explanation is a combination of several plausible contributing factors: on average somewhat smaller particles due to remaining pockets of aeolian dust, densification with depth through self compaction, and potentially increasing cementation with depth.

Acknowledgments

The design, building of, and research into the HP^3 has been supported by the German Aerospace Center DLR, United States National Aeronautics and Space Administration NASA, Austrian Academy of Sciences ÖAW, and the Polish Academy of Science CBK PAN. Part of this work was performed at the Jet Propulsion Laboratory, California Institute of Technology, under a contract with NASA. US government support acknowledged. RL acknowledges NASA InSight Participating Scientist grant 80NSSC18K1626. NA acknowledges support from the UK Space Agency, grant no. ST/R001375/2. The data are archived on the Planetary Data System (The InSight HP^3-RAD science team, 2018). This is InSight Contribution Number 138.

References

Acton, C. (1996, January). Ancillary data services of NASA's Navigation and Ancillary Information Facility. *Planetary and Space Science*, *44*(1), 65-70. doi: 10

.1016/0032-0633(95)00107-7

Acton, C., Bachman, N., Semenov, B., & Wright, E. (2018, January). A look towards the future in the handling of space science mission geometry. *Planetary and Space Science*, *150*, 9-12. doi: 10.1016/j.pss.2017.02.013

Banfield, D., Spiga, A., Newman, C., Forget, F., Lemmon, M., Lorenz, R., ... Banerdt, W. B. (2020, February). The atmosphere of Mars as observed by InSight. *Nature Geoscience*, *13*(3), 190-198. doi: 10.1038/s41561-020-0534-0

Betts, B. H., Murray, B. C., & Svitek, T. (1995, March). Thermal inertias in the upper millimeters of the Martian surface derived using Phobos' shadow. *Journal of Geophysical Research*, *100*(E3), 5285-5296. doi: 10.1029/95JE00226

Edwards, C. S., Piqueux, S., Hamilton, V. E., Fergason, R. L., Herkenhoff, K. E., Vasavada, A. R., ... Smith, M. D. (2018, May). The Thermophysical Properties of the Bagnold Dunes, Mars: Ground-Truthing Orbital Data. *Journal of Geophysical Research (Planets)*, *123*(5), 1307-1326. doi: 10.1029/2017JE005501

Fergason, R. L., Christensen, P. R., Bell, J. F., Golombek, M. P., Herkenhoff, K. E., & Kieffer, H. H. (2006, February). Physical properties of the Mars Exploration Rover landing sites as inferred from Mini-TES-derived thermal inertia. *Journal of Geophysical Research (Planets)*, *111*(E2), E02S21. doi: 10.1029/2005JE002583

Golombek, M., Kass, D., Williams, N., Warner, N., Daubar, I., Piqueux, S., ... Pike, W. T. (2020, August). Assessment of InSight Landing Site Predictions. *Journal of Geophysical Research (Planets)*, *125*(8), e06502. doi: 10.1029/2020JE006502

Golombek, M., Kipp, D., Warner, N., Daubar, I. J., Fergason, R., Kirk, R. L., ... Banerdt, W. B. (2017, October). Selection of the InSight Landing Site. *Space Science Reviews*, *211*(1-4), 5-95. doi: 10.1007/s11214-016-0321-9

Golombek, M., Warner, N. H., Grant, J. A., Hauber, E., Ansan, V., Weitz, C. M., ... Banerdt, W. B. (2020, February). Geology of the InSight landing site on Mars. *Nature Communications*, *11*, 1014. doi: 10.1038/s41467-020-14679-1

Gómez-Elvira, J., Armiens, C., Castañer, L., Domínguez, M., Genzer, M., Gómez, F., ... Martín-Torres, J. (2012, August). REMS: The Environmental Sensor Suite for the Mars Science Laboratory Rover. *Space Science Reviews*, *170*(1-4), 583-640. doi: 10.1007/s11214-012-9921-1

Grott, M., Spohn, T., Knollenberg, J., Krause, C., Hudson, T. L., Piqueux, S., … Banerdt, W. (2021). Thermal Conductivity of the Martian Soil at the InSight Landing site from HP^3 Active Heating Experiments. submitted to JGR-Planets.

Hamilton, V. E., Vasavada, A. R., Sebastián, E., Torre Juárez, M., Ramos, M., Armiens, C., … Zorzano, M.-P. (2014, April). Observations and preliminary science results from the first 100 sols of MSL Rover Environmental Monitoring Station ground temperature sensor measurements at Gale Crater. *Journal of Geophysical Research (Planets)*, *119*(4), 745-770. doi: 10.1002/2013JE004520

Kieffer, H. H. (2013, March). Thermal model for analysis of Mars infrared mapping. *Journal of Geophysical Research (Planets)*, *118*(3), 451-470. doi: 10.1029/2012JE004164

Lainey, V., Pasewaldt, A., Robert, V., Rosenblatt, P., Jaumann, R., Oberst, J., … Thuillot, W. (2020, December). Mars moon ephemerides after 12 years of Mars Express data. *Astronomy and Astrophysics*, *accepted*. doi: 10.1051/0004-6361/202039406

Lemmon, M. T., Guzewich, S. D., McConnochie, T., de Vicente-Retortillo, A., Martínez, G., Smith, M. D., … Jacob, S. (2019, August). Large Dust Aerosol Sizes Seen During the 2018 Martian Global Dust Event by the Curiosity Rover. *Geophysical Research Letters*, *46*(16), 9448-9456. doi: 10.1029/2019GL084407

Lorenz, R. D., Lemmon, M. T., Maki, J., Banfield, D., Spiga, A., Charalambous, C., … Banerdt, W. B. (2020, May). Scientific Observations With the InSight Solar Arrays: Dust, Clouds, and Eclipses on Mars. *Earth and Space Science*, *7*(5), e00992. doi: 10.1029/2019EA000992

Morgan, P., Grott, M., Knapmeyer-Endrun, B., Golombek, M., Delage, P., Lognonné, P., … Kedar, S. (2018, September). A Pre-Landing Assessment of Regolith Properties at the InSight Landing Site. *Space Science Reviews*, *214*(6), 104. doi: 10.1007/s11214-018-0537-y

Mueller, N. T., Knollenberg, J., Grott, M., Kopp, E., Walter, I., Krause, C., … Smrekar, S. (2020, May). Calibration of the HP^3 Radiometer on InSight. *Earth and Space Science*, *7*(5), e01086. doi: 10.1029/2020EA001086

Neckel, H., & Labs, D. (1994, August). Solar Limb Darkening 1986-1990 Lambda 303-NANOMETERS to 1099-NANOMETERS. *Solar Physics*, *153*(1-2), 91-114. doi: 10.1007/BF00712494

Piqueux, S., & Christensen, P. R. (2009a, September). A model of thermal conductivity for planetary soils: 1. Theory for unconsolidated soils. *Journal of Geophysical Research (Planets)*, *114*(E9), E09005. doi: 10.1029/2008JE003308

Piqueux, S., & Christensen, P. R. (2009b, September). A model of thermal conductivity for planetary soils: 2. Theory for cemented soils. *Journal of Geophysical Research (Planets)*, *114*(E9), E09006. doi: 10.1029/2008JE003309

Piqueux, S., & Christensen, P. R. (2012, November). Visible and thermal infrared observations of the Martian surface during three Phobos shadow transits. *Geophyiscal Research Letters*, *39*(21), L21203. doi: 10.1029/2012GL053352

Piqueux, S., Mueller, N., Grott, M., Siegler, M., Millour, E., Forget, F., … Banerdt, W. (2021). Soil Thermophysical Properties near the InSight Lander Derived from 50 Sols of Radiometer Measurements. submitted to JGR-Planets.

Presley, M. A., & Christensen, P. R. (1997a, January). The effect of bulk density and particle size sorting on the thermal conductivity of particulate materials under Martian atmospheric pressures. *Journal of Geophysical Research*, *102*(E4), 9221-9230. doi: 10.1029/97JE00271

Presley, M. A., & Christensen, P. R. (1997b, March). Thermal conductivity measurements of particulate materials 1. A review. *Journal of Geophysical Research*, *102*(E3), 6535-6550. doi: 10.1029/96JE03302

Presley, M. A., & Christensen, P. R. (1997c, March). Thermal conductivity measurements of particulate materials 2. results. *Journal of Geophysical Research*, *102*(E3), 6551-6566. doi: 10.1029/96JE03303

Spiga, A., Murdoch, N., Lorenz, R., Forget, F., Newman, C., Rodriguez, S., … Banerdt, W. B. (2021, January). A Study of Daytime Convective Vortices and Turbulence in the Martian Planetary Boundary Layer Based on Half-a-Year of InSight Atmospheric Measurements and Large-Eddy Simulations. *Journal of Geophysical Research (Planets)*, *126*(1), e06511. doi: 10.1029/2020JE006511

Spohn, T., Grott, M., Smrekar, S. E., Knollenberg, J., Hudson, T. L., Krause, C., … Banerdt, W. B. (2018, August). The Heat Flow and Physical Properties Package (HP^3) for the InSight Mission. *Space Science Reviews*, *214*(5), 96.

doi: 10.1007/s11214-018-0531-4

Stähler, S. C., Widmer-Schnidrig, R., Scholz, J. R., van Driel, M., Mittelholz, A., Hurst, K., ... Banerdt, W. B. (2020, October). Geophysical Observations of Phobos Transits by InSight. *Geophysical Research Letters*, *47*(19), e89099. doi: 10.1029/2020GL089099

The InSight HP^3-RAD science team. (2018). *Mars InSight Lander Radiometer Data Archive.* doi: 10.17189/1517568

Vasavada, A. R., Piqueux, S., Lewis, K. W., Lemmon, M. T., & Smith, M. D. (2017, March). Thermophysical properties along Curiosity's traverse in Gale crater, Mars, derived from the REMS ground temperature sensor. *Icarus*, *284*, 372-386. doi: 10.1016/j.icarus.2016.11.035

Viúdez-Moreiras, D., Newman, C. E., Forget, F., Lemmon, M., Banfield, D., Spiga, A., ... Grott, M. (2020, September). Effects of a Large Dust Storm in the Near-Surface Atmosphere as Measured by InSight in Elysium Planitia, Mars. Comparison With Contemporaneous Measurements by Mars Science Laboratory. *Journal of Geophysical Research (Planets)*, *125*(9), e06493. doi: 10.1029/2020JE006493

Willner, K., Shi, X., & Oberst, J. (2014, November). Phobos' shape and topography models. *Planetary and Space Science*, *102*, 51-59. doi: 10.1016/j.pss.2013.12.006

Supporting information for 'Near surface properties derived from Phobos transits with HP^3 RAD on InSight, Mars'

N. Mueller[1], S. Piqueux[2], M. Lemmon[3], J. Maki[2], R. D. Lorenz[4], M. Grott[1], T. Spohn[1,5], S.E. Smrekar[2], J. Knollenberg[1], T.L. Hudson[2], C. Krause[6], E. Millour[7], F. Forget[7], M. Golombek[2], A. Hagermann[8], N. Attree[9], M. Siegler[10], and W.B. Banerdt[2]

[1]Institute of Planetary Research, German Aerospace Center (DLR), Berlin, Germany

[2]Jet Propulsion Laboratory, California Institute of Technology, Pasadena, CA, USA

[3]Space Science Institute, College Station, TX, USA

[4]Johns Hopkins Applied Physics Laboratory, Laurel, MD, USA

[5]International Space Science Institute (ISSI), Bern, Switzerland

[6]Microgravity User Support Center, German Aerospace Center (DLR), Cologne, Germany

[7]Laboratoire de Météorologie Dynamique (LMD/IPSL), Sorbonne Université, Centre National de la Recherche Scientifique, École Polytechnique, École Normale Supérieure, Paris, France

[8]Luleå University of Technology, Space campus, Kiruna, Sweden

[9]Faculty of Natural Sciences, University of Stirling, Stirling, UK

[10]PSI, SMU Earth Science, Dallas, TX, USA.

Contents of this file

1. Text S1

2. Figures S1 to S4

Introduction

This supporting information provides the details of the numerical model of 1D heat conduction to calculate the temperature response to the transits of Phobos as observed by the InSight HP^3 Radiometer in text S1. The supporting figures S1 to S4 are modified versions of the Figures 2-3 in the main article showing all of the observed transits in comparison.

Text S1. The numerical calculation is based on the finite difference scheme in the work of (Kieffer, 2013), but modified to solve the equations implicitly. The finite difference equation is:

$$\frac{T_i - T_i'}{t - t'} = -\frac{H_{i+.5} - H_{i-.5}}{B_i \rho_i C_i} \tag{1}$$

where T is temperature, i indicates the i^{th} layer, t is time, a prime indicates the previous time-step, $H_{i+.5}$ indicates the heat flow through the top of the i^{th} layer,$H_{i-.5}$ same through the bottom, B is layer thickness, ρ is density, and C is specific heat capacity.

The temperatures of the top and bottom of layer interface, $T_{i-.5}$ and $T_{i+.5}$ respectively, are:

$$T_{i-.5} = T_i + \frac{H_{i-.5} B_i}{2k_i} \tag{2}$$

$$T_{i+.5} = T_i - \frac{H_{i+.5} B_i}{2k_i} \tag{3}$$

Calculating this interface starting from the layer below and substituting for $T_{i+.5}$ provides the interface heat flow (same approach for top of layer interface):

$$H_{i+.5} = \frac{-2(T_{i+1} - T_i)}{B_i/k_i + B_{i+1}/k_{i+1}} \tag{4}$$

$$H_{i-.5} = \frac{-2(T_i - T_{i-1})}{B_i/k_i + B_{i-1}/k_{i-1}} \tag{5}$$

At the uppermost layer ($i = 1$) the heat flow through the upper interface (the surface) is the boundary condition:

$$H_{.5} = (1 - a)H_{\mathrm{vis}} + e(H_{\mathrm{ir}} - \sigma_b T_{.5}^4) \tag{6}$$

Here a is visible albedo, H_{vis} incident visible band heat flux e is infrared emissivity, H_{ir} is infrared incident heat flux, and σ_b is the Stefan-Boltzmann constant. The incident heat fluxes are calculated using the KRC model (Kieffer, 2013) with the atmospheric opacity derived from imaging of the sky. At the lower boundary condition at $i = N$ the geothermal heat flow is $H_{N+0.5} = H_{geo}$. The geothermal heat flow is here assumed to be zero, since within the range of plausible values it is not significant for the observable temperature.

The solution of the set of non-linear implicit equations 1 is found by iteratively approaching the set of $N + 2$ temperatures $[T_{.5}, T_1, T_2, T_3, ...T_N, T_{N+.5}]$ that are the root of the function:

$$F_i = -\frac{H_{i+.5} - H_{i-.5}}{B_i \rho_i C_i} - \frac{T_i - T_i'}{t - t'} \tag{7}$$

using Broyden's method (Press et al., 1992). To reduce number of calculations per step this equation is simplified to:

$$F_i = \frac{2(T_{i+1} - T_i)}{B_i \rho_i C_i (\frac{B_i}{k_i} + \frac{B_{i+1}}{k_{i+1}})} - \frac{2(T_i - T_{i-1})}{B_i \rho_i C_i (\frac{B_i}{k_i} + \frac{B_{i-1}}{k_{i-1}})} - \frac{T_i - T_i'}{t - t'} \tag{8}$$

In the special case of the bottom and top layer centers ($i = 1, i = N$) the finite difference is evaluated at the surface and bottom interface, so half a layer thickness and constant parameters are assumed for the heat flow calculation:

$$H_{N+.5} = -\frac{2k_N(T_{N+.5} - T_N)}{B_N} \tag{9}$$

$$H_{1-.5} = -\frac{2k_1(T_1 - T_{.5})}{B_1} \tag{10}$$

Thus Eq. 7 is for these special cases:

$$F_1 = \frac{2(T_2 - T_1)}{B_1\rho_1 C_1(B_1/k_1 + B_2/k_2)} - \frac{2k_1(T_1 - T_{.5})}{B_1^2\rho_1 C_1} - \frac{T_1 - T_1'}{t - t'} \tag{11}$$

$$F_N = \frac{2k_N(T_{N+.5} - T_N)}{B_N^2\rho_1 C_1} - \frac{2(T_N - T_{N-1})}{B_N\rho_N C_N(B_N/k_N + B_{N-1}/k_{N-1})} - \frac{T_N - T_N'}{t - t'} \tag{12}$$

Further we define $\Delta t = t - t'$ and $G_i = F_i\Delta t$ and the following coefficients that are calculated once per model time-step based on the previous temperature state:

$$f_i = \frac{2\Delta t}{B_i\rho_i C_i(B_i/k_i + B_{i+1}/k_{i+1})}, \text{for } i = 1, ...N-1 \tag{13}$$

$$f_N = \frac{2k_N\Delta t}{B_N^2\rho_1 C_1} \tag{14}$$

$$b_i = \frac{2\Delta t}{B_i\rho_i C_i(B_i/k_i + B_{i-1}/k_{i-1})}, \text{for } i = 2, ...N \tag{15}$$

$$b_1 = \frac{2k_1\Delta t}{B_1^2\rho_1 C_1} \tag{16}$$

With the notation for the sake of simplicity of implementation: $T_0 = T_{0.5}$ and $T_{N+1} = T_{N+0.5}$ the equation for root finding is then:

$$G_i = f_i(T_{i+1} - T_i) - b_i(T_i - T_{i-1}) - T_i + T_i', \text{for } i = 1, ...N \tag{17}$$

The top and bottom temperatures T_0 and T_N+1 are determined by the heat flow boundary conditions:

$$G_0 = \frac{2k_1(T_1 - T_0)}{B_1} + (1-a)H_{\text{vis}} + e(H_{\text{ir}} - \sigma_b T_0^4) - h_{\text{conv}} T_0 \tag{18}$$

$$G_{N+1} = \frac{2k_N(T_{N+1} - T_N)}{B_N} + H_{geo} \tag{19}$$

Broyden's method iterates solutions to Eq. 17 and Eq. 18 to find of $N+2$ temperatures T_i for which G_i converges to zero.

References

Kieffer, H. H. (2013, March). Thermal model for analysis of Mars infrared mapping. *Journal of Geophysical Research (Planets)*, *118*(3), 451-470. doi: 10.1029/2012JE004164

Press, W., Teukolsky, S., Vetterling, W., & Flannery, B. (1992). *Numerical Recipes in C* (2nd ed.). Cambridge, UK: Cambridge University Press.

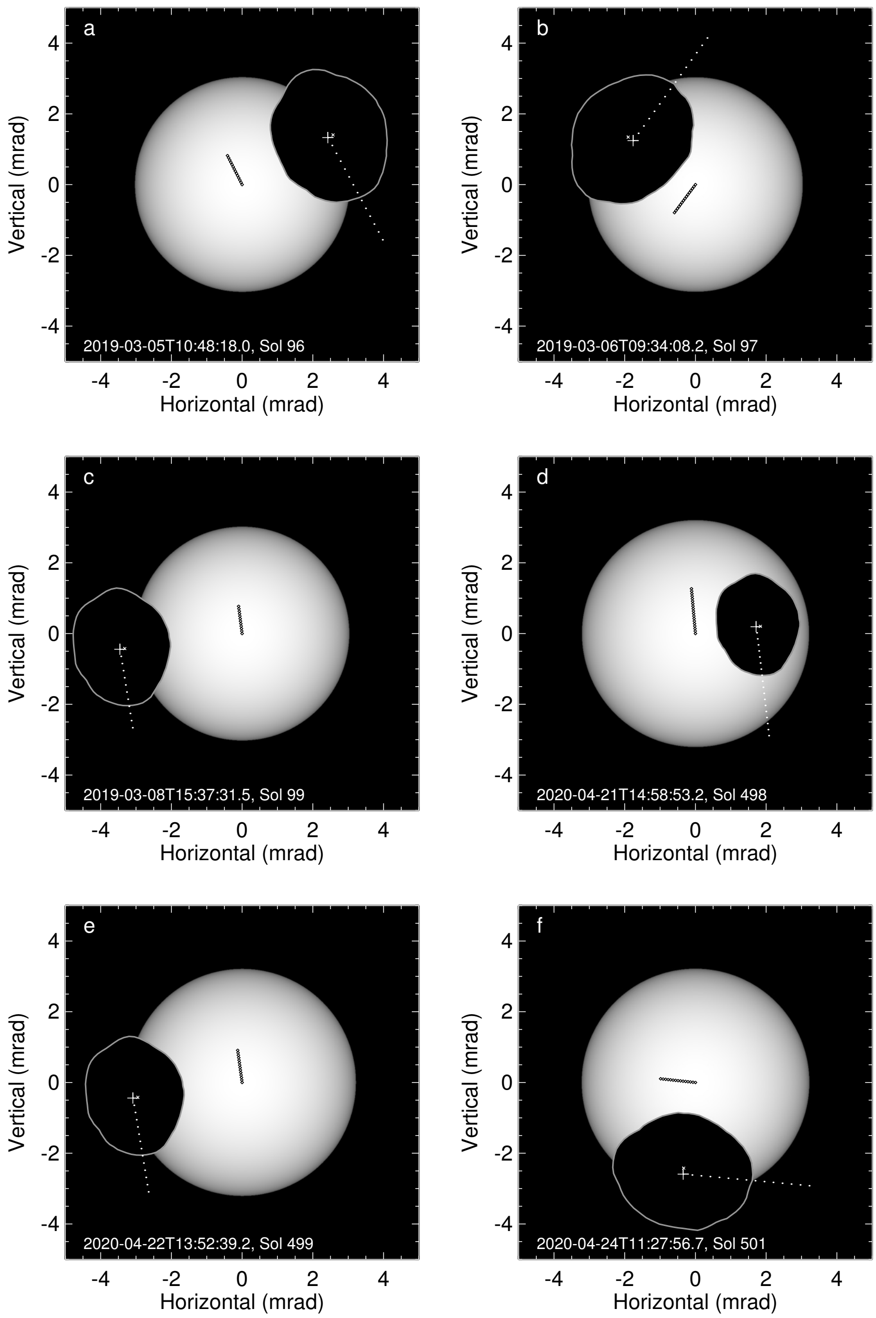

Figure S1. Simulated images of the moment of smallest angular separation of Phobos and Sun of all transits. The white + symbol indicates the Phobos Barycenter position, while the smaller x symbol indicates an offset of the Phobos barycenter for 1 km along the rotation axis towards the north pole.

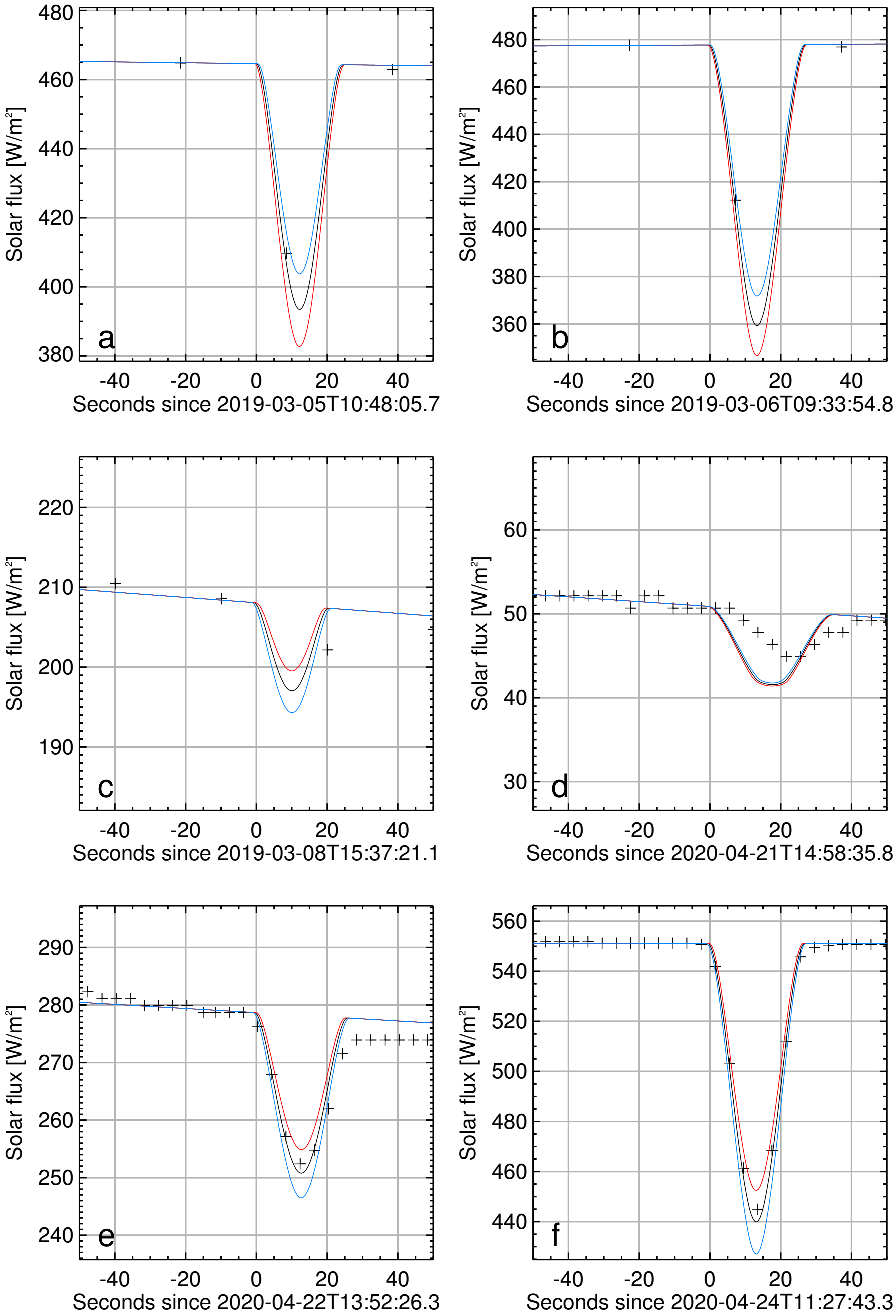

Figure S2. The simulated lightcurves in comparison to scaled solar panel currents for all transits. The symbols represent readings of the solar panel currents and the solid curves correspond to modeled lightcurves, where the blue and red curves correspond to position of Phobos that is ± 1 km offset along its rotation axis.

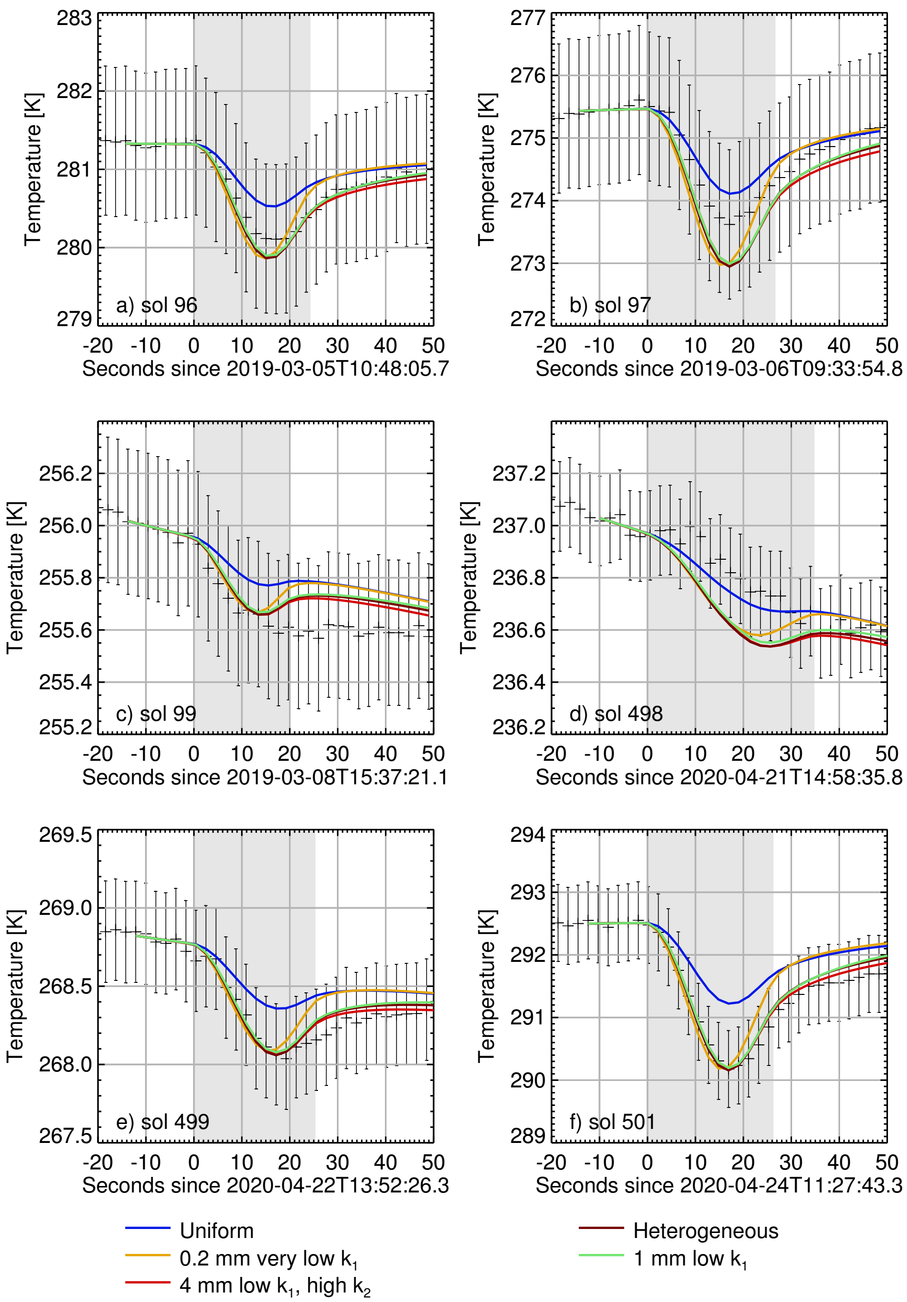

Figure S3. The temperature response of the surface during all transits observed by RAD together with several models for comparison. An offset is added to each model so that the data and model temperatures match on average in the 20 seconds preceding the transit. The model parameter details are described in the text of the main article.

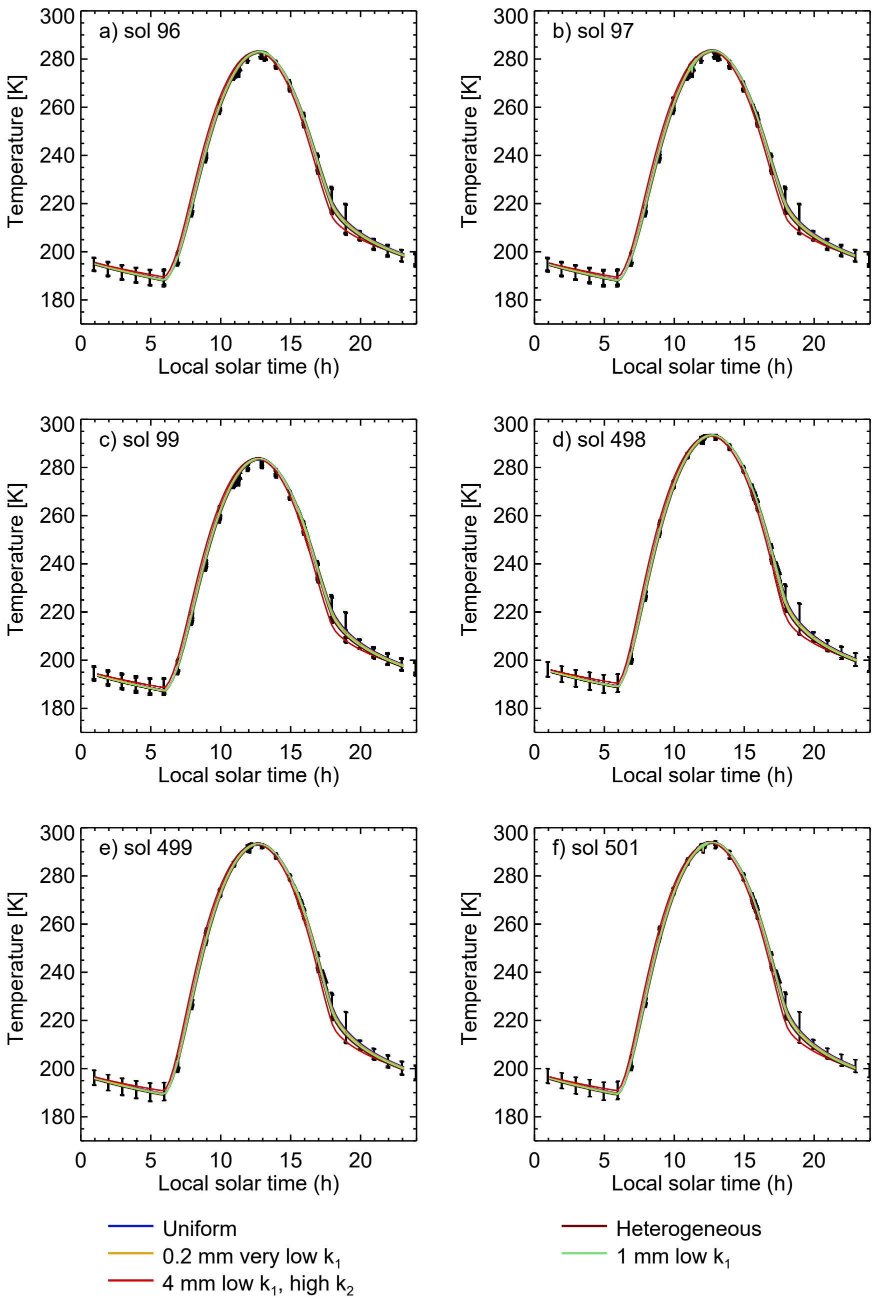

Figure S4. The diurnal surface temperatures observed within 3 sols of each transit. The error bars are total uncertainty of the radiometer which is mostly related to calibration uncertainty with only a minor contribution from atmospheric noise. Also plotted are the same models as described in the text of the main article.